

Cooperative Catalytic Effect of ZrO₂ and α-Fe₂O₃ Nanoparticles on BiVO₄ Photoanodes for Enhanced Photoelectrochemical Water Splitting

Maged N. Shaddad,^[b] Mohamed A. Ghanem,^[b] Abdullah M. Al-Mayouf,^[b] Sixto Gimenez,^[a] Juan Bisquert,^{*,[a, b]} and Isaac Herraiz-Cardona^{*,[a]}

Photoelectrochemical water splitting with metal oxide semiconductors offers a cost-competitive alternative for the generation of solar fuels. Most of the materials studied so far suffer from poor charge-transfer kinetics at the semiconductor/liquid interface, making compulsory the use of catalytic layers to overcome the large overpotentials required for the water oxidation reaction. Herein, we report a very soft electrolytic synthesis deposition method, which allows remarkably enhanced water oxidation kinetics of BiVO₄ photoanodes by the sequential addition of Zr and Fe precursors. Upon a heat treatment cycle, these precursors are converted into monoclinic ZrO₂ and α-Fe₂O₃ nanoparticles, which mainly act as catalysts, leading to a five-fold increase of the water oxidation photocurrent of BiVO₄. This method provides a versatile platform that is easy to apply to different semiconductor materials, fully reproducible, and facile to scale-up on large area conductive substrates with attractive implications for technological deployment.

Photoelectrochemical (PEC) water splitting driven by sunlight constitutes an environmentally friendly technology to store energy in the covalent bonds of H₂.^[1] To efficiently convert solar photons into such a chemical fuel, semiconducting materials capable of absorbing a large fraction of the solar spectrum, with an adequate band edge position, and low overpotentials to carry out the hydrogen and/or oxygen evolution reactions are required. In particular, intensive research efforts have been accomplished to develop competitive n-type semiconducting materials working as water splitting photoanodes, as the oxygen evolution reaction (OER) is both kinetically and thermodynamically more demanding,^[2] and the material suffers from severe oxidizing conditions.

To achieve cost-competitive, efficient, and durable devices, the use of low-cost, earth-abundant, stable materials synthe-

sized by easily up-scalable methods is essential. In this context, metal oxides, such as monoclinic BiVO₄ (m-BiVO₄)^[3] and α-Fe₂O₃,^[4] have been deeply investigated as candidate photoanode materials. Although both of them satisfy many of the requirements, their poor electronic properties yield low solar-to-fuel efficiencies, preventing their large-scale use in PEC systems at present. To overcome this problem, different strategies have been implemented, including ion doping,^[3d, g, 4a, c, 5] nanostructuring,^[3a, f, 4a, 6] surface modification with passivation layers or electrocatalysts,^[3b, d, 5d, 7] and combinatorial synthesis.^[8] For example, α-Fe₂O₃ photoanodes have been successfully doped with heteroatoms like Sn,^[5a] Ti,^[4c] Zr,^[5b, c] Si,^[4a] and Nb.^[5d] In the case of monoclinic BiVO₄ (m-BiVO₄), there are two different sites susceptible to metal doping, that is, Bi³⁺ and V⁵⁺. Whereas the replacement of V⁵⁺ sites by six valence metal ions, such as Mo and W,^[3d, 5e, f] has been largely explored, there are very few studies on doping Bi³⁺ sites, and are generally limited to theoretical calculations.^[9] Hf⁴⁺, Zr⁴⁺, and Sn⁴⁺, with ion radius relatively similar to Bi³⁺, are potential candidates to occupy Bi positions in the m-BiVO₄ crystal structure. Luo et al.^[10] synthesized BiVO₄ photoanodes doped by Sn⁴⁺ in Bi³⁺ positions by means of a metal-organic decomposition (MOD) method. A practically negligible improvement in photocurrent was reported for the doped sample, which was attributed to the high formation energy and the relatively low solubility of Sn⁴⁺ impurity ions into the crystal lattice.

The functional properties of BiVO₄ and Fe₂O₃ have also been separately improved by means of heterostructuring strategies. For instance, the PEC performance of BiVO₄ has been largely increased when deposited on nanostructured WO₃ layers, owing to the synergistic interaction between the BiVO₄ (providing good light harvesting properties) and WO₃ (enhanced charge transport).^[3f, 11] Other different host-guest semiconductor combinations have been successfully implemented and tested with remarkable results for water splitting, like Si/TiO₂/BiVO₄,^[12] SnO₂/BiVO₄,^[13] WO₃/Fe₂O₃,^[14] and Si/Fe₂O₃.^[15]

Nevertheless, to the best of our knowledge, the heterostructured Fe₂O₃/BiVO₄ system, which would entirely match the stability and low-cost requirements, has not been tested for solar water oxidation. There is only one recent work in literature reporting the decoration of BiVO₄ with Fe₂O₃ nanoparticles, where it is suggested that Fe₂O₃ acts as an efficient co-catalyst for the degradation of organic pollutants.^[16] Although different Fe-based catalysts have been successfully employed to decorate semiconductor photoanodes, such as FeOOH^[7a] and Ni-

[a] S. Gimenez, J. Bisquert, I. Herraiz-Cardona
Institute of Advanced Materials (INAM)
Universitat Jaume I
12006 Castelló (Spain)
E-mail: bisquert@uji.es
iherraiz@uji.es

[b] M. N. Shaddad, M. A. Ghanem, A. M. Al-Mayouf, J. Bisquert
Department of Chemistry, Faculty of Science
King Saud University
Riyadh (Saudi Arabia)

Supporting Information and the ORCID identification number(s) for the author(s) of this article can be found under <http://dx.doi.org/10.1002/cssc.201600890>.

FeO_x ^[3a,17] the use of $\alpha\text{-Fe}_2\text{O}_3$ nanoparticles as OER catalyst has not been explored.

Herein, we report a very soft electrolytic synthesis deposition method that is fully reproducible and facile to scale-up on large area conductive substrates, which allows enhancing remarkably the water oxidation kinetics of BiVO_4 photoanodes by the sequential addition of Zr and Fe precursors.

BiVO_4 photoanodes were synthesized by means of the two-step method developed by Choi et al.,^[3c] which consisted of Bi electrodeposition on a fluorine-doped tin oxide (FTO) substrate followed by drop casting the V precursor and annealing at 500 °C for 2 h. Different amounts of $\text{Zr}_2\text{Cl}_2\text{O}$ were incorporated into the Bi^{3+} plating bath as the source of Zr. Subsequently, electrodeposition of Fe on the as-prepared BiVO_4 layers followed by annealing at 450 °C was carried out to obtain Fe_2O_3 nanoparticles. Different electrodeposition charges were tested, ranging from 1 to 32 mC cm^{-2} . After systematic optimization of the deposition process, a five-fold increase of the water oxidation photocurrent at 1.23 V versus RHE was obtained compared to the reference BiVO_4 system. Figure 1 illustrates the photoelectrochemical behavior of the reference Fe_2O_3 (A) and BiVO_4 (B) photoanodes together with the best modified BiVO_4 electrodes: $\text{BiVO}_4\text{-Zr}$ (C), $\text{BiVO}_4\text{-Fe}$ (D), and $\text{BiVO}_4\text{-Zr-Fe}$ (E). The photocurrents at 1.23 V versus RHE for the different Zr and Fe additions are showed in Figure 1b and are used to determine the optimum synthetic conditions reported in Figure 1a. Typical volcano plots for both Zr and Fe additions on top of the BiVO_4 surface were obtained. The best performance was obtained for 2.5 mole% Zr. Note that this concentration is referred to the Zr/Bi molar ratio added to the electrodeposition bath. On the other hand, 2 mC cm^{-2} of total charge deposition of Fe yielded the optimum results. Although the photocurrents reported in Figure 1 are lower compared to previous studies on BiVO_4 photoanodes,^[3a,b,7a] the efficiency is remarkably enhanced by the Zr and Fe additions compared with the reference material. Additionally, the simplicity of the method described here to engineer surface modifications can be mimicked in more efficient systems. Figure 1c shows the j - V curves when a hole scavenger (1 M Na_2SO_3) was added to the solution.

In general, all BiVO_4 -based samples exhibit practically the same behavior for sulfite oxidation when surface recombination is negligible, with photocurrents slightly higher than reported for oxygen evolution. This strongly suggests that the improvement reported for the optimized $\text{BiVO}_4\text{-Zr-Fe}$ photoanode is mainly connected to surface catalysis.

To more precisely determine the role of both additives (Zr and Fe) on the PEC behavior of the photoelectrodes, detailed structural and optical characterization was performed. First, XRD measurements of the metallic deposits were carried out (see Figure SI1 in the Supporting Information). The results show that as the Zr content increases, the intensity of the peak assigned for Bi at $2\theta = 27.5^\circ$ diminishes, which indicates that Bi-Zr codeposition was successfully accomplished. In addition, SEM images of as-deposited metals (Figure SI2) show a progressive morphological evolution with increased Zr additions, from dendrite trunks and branches (pure Bi deposits) to more compact films. Figure 2a and b show the SEM micrographs of pristine BiVO_4 and $\text{BiVO}_4\text{-Zr}$, with the optimum Zr addition (2.5 mol%), illustrating that after the vanadate formation process, the microstructure of the samples considerably changes to smoother-edged dendrites, although a high surface area is maintained. Furthermore, it is remarkable the decrease of the nanoparticle size from approximately 500 nm for pristine BiVO_4 to 200 nm for the optimized $\text{BiVO}_4\text{-Zr}$ electrode. This is consistent with the role of Zr as grain growth inhibitor as reported for different metallurgical synthetic processes.^[18] Figure 2c shows the XRD diffractograms of $\text{BiVO}_4\text{-Zr}$ samples for different Zr additions, perfectly matching the monoclinic scheelite BiVO_4 structure (CAS Number 00-014-0688). The intensity of the (121) peak increases with the Zr concentration up to the optimum 2.5 mol%, and is practically unchanged with further Zr additions. Moreover, the peak position shifts toward higher 2θ values for the most Zr-rich samples. This clearly involves a degradation of the film integrity as a result of the strain induced by the smaller ionic radius of Zr (0.79 Å) replacing Bi^{3+} positions (1.11 Å) into the periodic crystal lattice,^[5g] which can be related to the progressive decrease of the photocurrent showed in Figure 1b for the higher Zr additions.

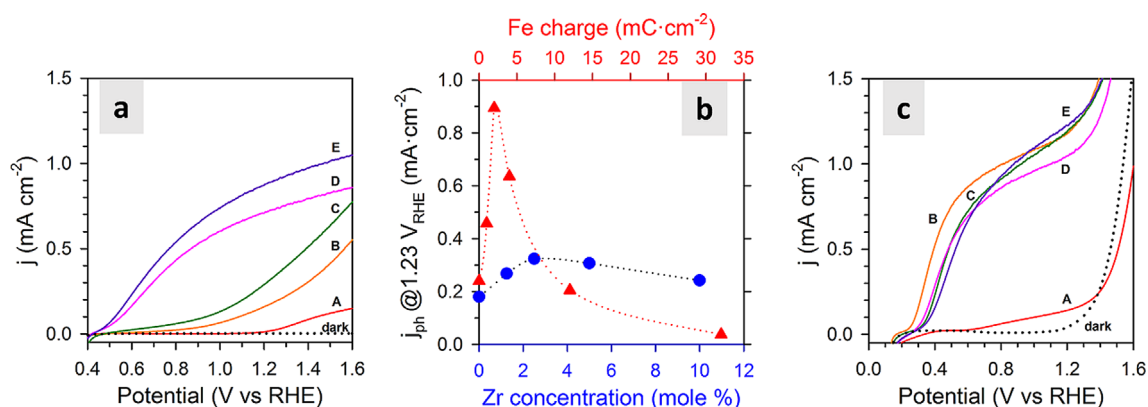


Figure 1. j - V curves of the synthesized films obtained in the dark (dashed lines) and under illumination at 100 mW cm^{-2} (solid lines) in phosphate buffer solution at pH 7.6 (a) without and (c) with a hole scavenger (1 M Na_2SO_3) in the solution. (b) Photocurrents obtained at 1.23 V vs. RHE for different Zr (blue symbols) and Fe (red symbols) additions in the phosphate buffer solution at pH 7.6. Labelled samples correspond to reference (A) $\alpha\text{-Fe}_2\text{O}_3$ and (B) BiVO_4 , and optimized (C) $\text{BiVO}_4\text{-Zr}$, (D) $\text{BiVO}_4\text{-Fe}$, and (E) $\text{BiVO}_4\text{-Zr-Fe}$ photoanodes, respectively.

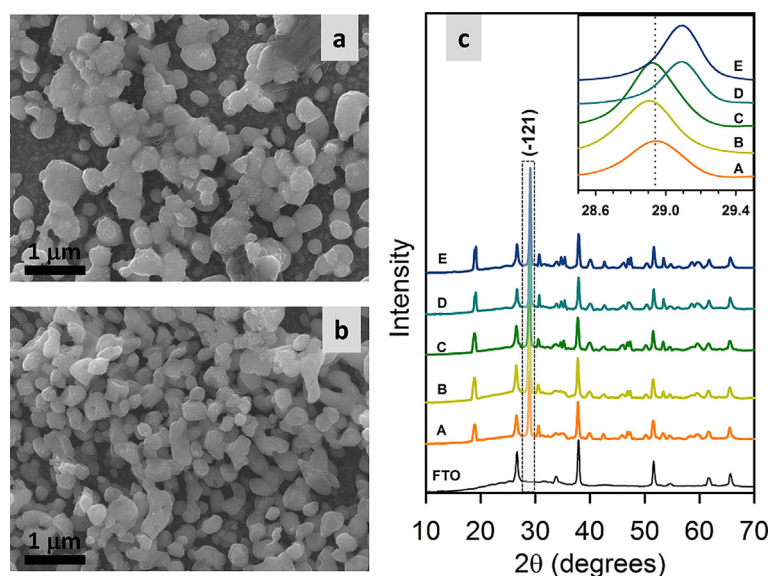


Figure 2. SEM images of (a) pristine and (b) after 2.5 mole% Zr addition to BiVO_4 films. (c) XRD patterns of pristine and modified BiVO_4 nanopowders with different Zr loadings. Labelled samples correspond to reference (A) BiVO_4 and (B) 1.25, (C) 2.5, (D) 5, and (E) 10% BiVO_4 -Zr, respectively. The zoomed area shows the displacement of 2θ for the peak corresponding to the $(\bar{1}21)$ plane.

Figure 3 shows HR-TEM images of the optimized BiVO_4 -Zr and BiVO_4 -Zr-Fe photoanodes. The BiVO_4 -Zr electrodes are characterized by the presence of high crystalline nanoparticles (5–10 nm), with interplanar distances of 2.8 Å (Figure 3 a) and 3.1 Å (Figure 3 b) corresponding to the (111) and $(\bar{1}11)$ reflections of monoclinic ZrO_2 (CAS Number 1309-37-1), respectively. Local energy dispersive X-ray spectroscopy (EDS) analyses confirmed the presence of Zr at these locations (Figure SI3), clearly

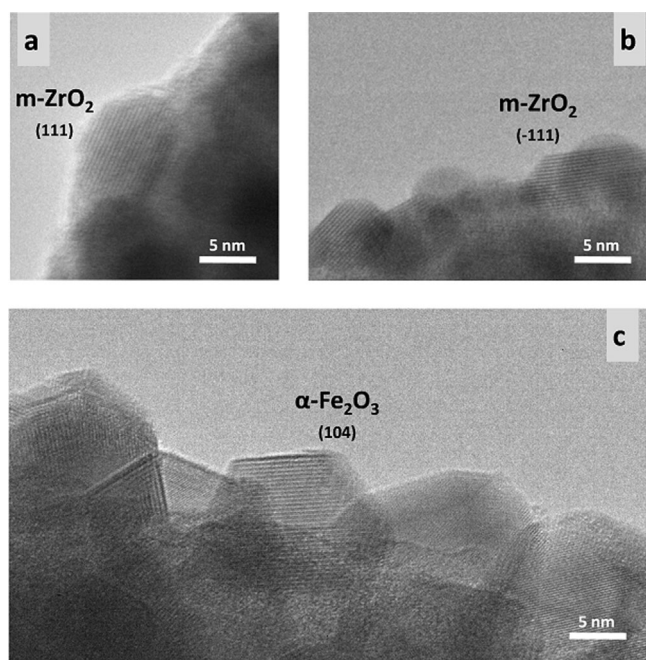


Figure 3. High resolution TEM images of optimized (a–b) BiVO_4 -Zr photoanodes (2.5% Zr addition) and (c) BiVO_4 -Zr-Fe electrodes (2.5 mole% Zr addition and electrodeposition of 2 mC cm^{-2} of Fe). In all images, lattice parameters were determined by the lattice fringes of the nanoparticles pointed by the arrows.

indicating that although Zr can substitute Bi in the monoclinic BiVO_4 lattice as showed by XRD, an important fraction of Zr is present at the surface of BiVO_4 in the form of monoclinic ZrO_2 nanoparticles. The formation of ZrO_2 nanoparticles upon Zr addition has been reported even for low doping densities, below 1 at%.^[19] On the other hand, the optimized BiVO_4 -Zr-Fe samples, additionally showed the presence of crystalline nanoparticles, with interplanar distances of 2.7 Å (Figure 3 c), corresponding to the (104) reflections of hexagonal scalenohedral $\alpha\text{-Fe}_2\text{O}_3$, (CAS Number 1309-37-1) that appeared homogeneously dispersed on top of the BiVO_4 -Zr photoanode.

The optical properties of BiVO_4 were not significantly altered by Zr additions, as showed in the Supporting Information (Figure SI4 a), in good agreement with previous reports.^[9] According to its bandgap of 2.4 eV, BiVO_4 is able to absorb light up to approximately 510 nm. On the other hand, as the amount of electrodeposited Fe increases, a broad shoulder appears on the 500–650 nm region, matching the main absorption band of $\alpha\text{-Fe}_2\text{O}_3$ (Figure SI4 b). A clear visual effect of the electrodeposition of different amounts of Fe can be observed in Figure SI5. At the highest Fe loading, the yellowish BiVO_4 substrate is completely covered and the samples have an orange/reddish color, characteristic of Fe_2O_3 .

The estimated optical bandgaps (E_g) of the heterostructured materials were extracted from the Tauc plots for direct bandgap transitions (Figure SI4 c). The obtained values are approximately 2.40 eV for pristine and BiVO_4 -Zr samples, in good agreement with those previously reported. A progressive decrease of the bandgap energy with the addition of Fe was detected, from an electrodeposition charge of 12 mC cm^{-2} , obtaining $E_g = 2.32 \text{ eV}$ for the highest Fe loading tested (i.e., 32 mC cm^{-2}), in good agreement with the optical properties of $\alpha\text{-Fe}_2\text{O}_3$. From these optical absorption measurements, the maximum achievable photocurrent was calculated considering

that all the photogenerated holes participate in the water oxidation reaction (j_{abs}), see Table S11.

The enhanced PEC activity induced by the Zr and Fe additions was further corroborated by the incident photon-to-current efficiency (IPCE) spectra obtained at 1.23 V versus RHE without and with the addition of the hole scavenger (Figure 4a and b, respectively). There is an excellent correspondence between the onset wavelength of the IPCE and the absorbance measurements. Moreover, the integrated photocurrents extracted from the IPCE spectra nicely match those obtained from the j - V curves, as summarized in Table S11. From the IPCE measurements in the solution with the hole scavenger, it is clear that the enhanced PEC behavior for the optimized heterostructure can be ascribed to the “cooperative” (rather than synergistic) catalytic effect of both ZrO_2 and $\alpha\text{-Fe}_2\text{O}_3$ nanoparticles deposited on the top of the m-BiVO_4 films. Evidence of the excellent electrocatalytic behavior of $\alpha\text{-Fe}_2\text{O}_3$ has been previously reported for Si photoanodes.^[20] Conversely, nanostructured monoclinic ZrO_2 nanoparticles have demonstrated catalytic activity for different chemical reactions,^[21] and has been also employed to passivate TiO_2 surface traps in dye-sensitized solar cells.^[22] However, to the best of the authors knowledge it is the first time that they show enhanced water oxidation kinetics.

To quantitatively assess the beneficial effect of both Zr and Fe additions on BiVO_4 films, the charge separation (η_{cs}) and

charge injection (η_{cat}) yields were calculated for the synthesized materials through Equations (1) and (2), by comparing the photocurrent for water splitting and to a hole scavenger:^[23]

$$j_{\text{H}_2\text{O}} = j_{\text{abs}} \times \eta_{\text{cs}} \times \eta_{\text{cat}} \quad (1)$$

$$j_{\text{HS}} = j_{\text{abs}} \times \eta_{\text{cs}} \quad (2)$$

The comparative behavior of both calculated yields is showed in Figure 5. When Fe is distributed in the form of scattered Fe_2O_3 nanoparticles on the BiVO_4 surface, this material acts as an excellent catalyst for oxygen evolution reaction, doubling the catalytic efficiency of the semiconductor substrate. It is also remarkable the increase in the catalytic efficiency of BiVO_4 -Zr samples, with respect to the reference BiVO_4 . In contrast, the effect of Zr addition on the charge separation efficiency is negligible, in good agreement with previous reports suggesting that Zr additions on BiVO_4 do not affect the electronic properties of the material.^[3e,9] The validity of this analysis is based on the assumption of complete absence of surface recombination when the hole scavenger is employed. A marginal difference is observed in the measurements with the hole scavenger, which can be attributed to the role of ZrO_2 and $\alpha\text{-Fe}_2\text{O}_3$ as surface passivation layers on top of BiVO_4 .^[7b] In any case, further analysis is needed to clarify this issue.

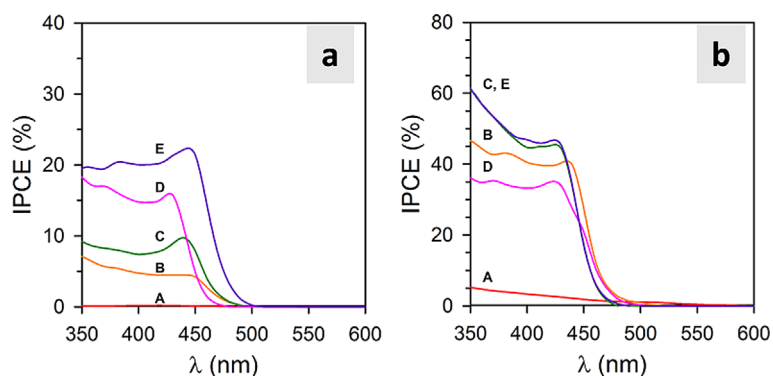


Figure 4. IPCE spectra obtained on the synthesized films at 1.23 V vs. RHE in phosphate buffer solution at pH 7.6 (a) without and (b) with hole scavenger (1 M Na_2SO_3). Labelled samples correspond to (A) $\alpha\text{-Fe}_2\text{O}_3$, (B) reference BiVO_4 , and optimized (C) BiVO_4 -Zr, (D) BiVO_4 -Fe, and (E) BiVO_4 -Zr-Fe photoanodes, respectively.

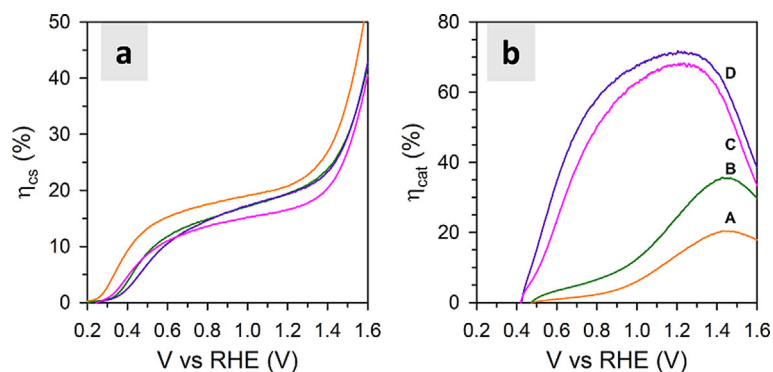


Figure 5. (a) Charge-separation efficiency and (b) charge-injection efficiency obtained on the synthesized films. Labelled samples correspond to (A) reference BiVO_4 and optimized (B) BiVO_4 -Zr, (C) BiVO_4 -Fe, and (D) BiVO_4 -Zr-Fe samples, respectively.

Figure S16 shows the Mott–Schotky plots obtained in the dark on BiVO₄ and optimized BiVO₄-Zr and BiVO₄-Zr-Fe samples. The lower slope reported for the BiVO₄-Zr samples is connected to an increase in the surface area as shown in Figure 2, rather than to an increase in donor density. The material roughness is further increased for the BiVO₄-Zr-Fe sample, which can explain the lowest slope in the Mott–Schotky plot of Figure S16, as a consequence of the Fe₂O₃ nanoparticle decoration and/or the ZrO₂ morphological rearrangement on top of BiVO₄ photoanode under the second annealing.^[24] The calculated flat band potentials (V_{fb}) and donor densities (N_D) are collected in Table S12. No significant changes are obtained for the electronic properties of BiVO₄ upon Zr and Fe additions, as reflected in the charge separation yield in Figure 5a.

To benchmark the cooperative catalytic Zr–Fe-based layer developed in the present study, we have compared the reported behavior with that obtained with a FeOOH catalyst. For this purpose, we have deposited a FeOOH layer on top of our BiVO₄ photoanode, according to the optimum synthesis conditions described by Seabold and Choi in Ref. [7a]. Figure S17 shows both the photoelectrochemical and optical properties of both systems. Our BiVO₄-Zr-Fe photoanode clearly outperforms BiVO₄-FeOOH in terms of delivered photocurrent. Additionally, the absorbance of our catalytic layer is significantly lower, which is particularly beneficial for application in tandem architectures.

In summary, we have reported a facile method to enhance the PEC water oxidation behavior of BiVO₄ photoanodes by controlled additions of Zr and Fe precursors on the electrodeposition bath. A remarkable five-fold increase of the photocurrent is reported for the optimized BiVO₄-Zr-Fe photoanodes, which can be explained by the cooperative catalytic role of monoclinic ZrO₂ and α -Fe₂O₃ nanoparticles distributed on the surface of BiVO₄. Although we show by XRD analysis that Zr can also extrinsically dope BiVO₄ replacing Bi atoms, the effect on the intrinsic electronic properties of BiVO₄ is not beneficial for the optimum Zr addition. The findings of this study can also be easily extrapolated to enhance the PEC performance of different photoanode materials with low-cost catalytic materials like Fe₂O₃ and ZrO₂, obtained by a simple, fully reproducible, and up-scalable synthesis.

Acknowledgements

We thank financial support from the University Jaume I through the project P1-1B2011-50. Serveis Centrals at UJI (SCIC) are also acknowledged.

Keywords: electrolytic synthesis · nanoparticles · photoanode · water oxidation kinetics · water splitting

[1] M. G. Walter, E. L. Warren, J. R. McKone, S. W. Boettcher, Q. Mi, E. A. Santori, N. S. Lewis, *Chem. Rev.* **2010**, *110*, 6446–6473.

[2] J. Tang, J. R. Durrant, D. R. Klug, *J. Am. Chem. Soc.* **2008**, *130*, 13885–13891.

- [3] a) Y. Kuang, Q. Jia, H. Nishiyama, T. Yamada, A. Kudo, K. Domen, *Adv. Energy Mater.* **2016**, *6*, 1501645; b) T. W. Kim, K.-S. Choi, *Science* **2014**, *343*, 990–994; c) D. Kang, Y. Park, J. C. Hill, K.-S. Choi, *J. Phys. Chem. Lett.* **2014**, *5*, 2994–2999; d) F. F. Abdi, N. Firet, R. van de Krol, *ChemCatChem* **2013**, *5*, 490–496; e) W. Luo, Z. Yang, Z. Li, J. Zhang, J. Liu, Z. Zhao, Z. Wang, S. Yan, T. Yu, Z. Zou, *Energy Environ. Sci.* **2011**, *4*, 4046–4051; f) X. Shi, Y. Choi, K. Zhang, J. Kwon, D. Y. Kim, J. K. Lee, S. H. Oh, J. K. Kim, J. H. Park, *Nat. Commun.* **2014**, *5*, 4775; g) F. F. Abdi, L. Han, A. H. M. Smets, M. Zeman, B. Dam, R. van de Krol, *Nat. Commun.* **2013**, *4*, 2195.
- [4] a) A. Kay, I. Cesar, M. Grätzel, *J. Am. Chem. Soc.* **2006**, *128*, 15714–15721; b) C. Du, X. Yang, M. T. Mayer, H. Hoyt, J. Xie, G. McMahon, G. Bischooping, D. Wang, *Angew. Chem. Int. Ed.* **2013**, *52*, 12692–12695; *Angew. Chem.* **2013**, *125*, 12924–12927; c) O. Zandi, B. M. Klahr, T. W. Hamann, *Energy Environ. Sci.* **2013**, *6*, 634–642.
- [5] a) C. D. Bohn, A. K. Agrawal, E. C. Walter, M. D. Vaudin, A. A. Herzing, P. M. Haney, A. A. Talin, V. A. Szalai, *J. Phys. Chem. C* **2012**, *116*, 15290–15296; b) S. Shen, *J. Mater. Res.* **2014**, *29*, 29–46; c) P. Kumar, P. Sharma, R. Shrivastav, S. Dass, V. R. Satsangi, *Int. J. Hydrogen Energy* **2011**, *36*, 2777–2784; d) L. Steier, I. Herraiz-Cardona, S. Gimenez, F. Fabregat-Santiago, J. Bisquert, S. D. Tilley, M. Grätzel, *Adv. Funct. Mater.* **2014**, *24*, 7681–7688; e) K. P. S. Parmar, H. J. Kang, A. Bist, P. Dua, J. S. Jang, J. S. Lee, *ChemSusChem* **2012**, *5*, 1926–1934; f) H. S. Park, K. E. Kweon, H. Ye, E. Paek, G. S. Hwang, A. J. Bard, *J. Phys. Chem. C* **2011**, *115*, 17870–17879; g) J. D. Bryan, D. R. Gamelin, *Prog. Inorg. Chem.* **2005**, *54*, 47–126.
- [6] F. E. Osterloh, *Chem. Soc. Rev.* **2013**, *42*, 2294–2320.
- [7] a) J. A. Seabold, K.-S. Choi, *J. Am. Chem. Soc.* **2012**, *134*, 2186–2192; b) Y. Ma, A. Kafizas, S. R. Pendlebury, F. Le Formal, J. R. Durrant, *Adv. Funct. Mater.* **2016**, 4951–4960; c) D. K. Zhong, S. Choi, D. R. Gamelin, *J. Am. Chem. Soc.* **2011**, *133*, 18370–18377.
- [8] C. Jiang, R. Wang, B. A. Parkinson, *ACS Comb. Sci.* **2013**, *15*, 639–645.
- [9] a) Z. Zhao, W. Luo, Z. Li, Z. Zou, *Phys. Lett. A* **2010**, *374*, 4919–4927; b) W.-J. Yin, S.-H. Wei, M. M. Al-Jassim, J. Turner, Y. Yan, *Phys. Rev. B* **2011**, *83*, 155102.
- [10] W. Luo, J. Wang, X. Zhao, Z. Zhao, Z. Li, Z. Zou, *Phys. Chem. Chem. Phys.* **2013**, *15*, 1006–1013.
- [11] a) X. Shi, I. Herraiz-Cardona, L. Bertoluzzi, P. Lopez-Varo, J. Bisquert, J. H. Park, S. Gimenez, *Phys. Chem. Chem. Phys.* **2016**, *18*, 9255–9261; b) I. Grigioni, K. G. Stamplecoskie, E. Selli, P. V. Kamat, *J. Phys. Chem. C* **2015**, *119*, 20792–20800.
- [12] H. Jung, S. Y. Chae, C. Shin, B. K. Min, O.-S. Joo, Y. J. Hwang, *ACS Appl. Mater. Interfaces* **2015**, *7*, 5788–5796.
- [13] P. Chatchai, Y. Murakami, S.-y. Kishioka, A. Y. Nosaka, Y. Nosaka, *Electrochem. Solid-State Lett.* **2008**, *11*, H160–H163.
- [14] K. Sivula, F. L. Formal, M. Grätzel, *Chem. Mater.* **2009**, *21*, 2862–2867.
- [15] M. T. Mayer, Y. Lin, G. Yuan, D. Wang, *Acc. Chem. Res.* **2013**, *46*, 1558–1566.
- [16] P. Cai, S.-M. Zhou, D.-K. Ma, S.-N. Liu, W. Chen, S.-M. Huang, *Nano-Micro Lett.* **2015**, *7*, 183–193.
- [17] J. E. Thorne, S. Li, C. Du, G. Qin, D. Wang, *J. Phys. Chem. Lett.* **2015**, *6*, 4083–4088.
- [18] a) K. He, T. N. Baker, *Mater. Sci. Eng. A* **1998**, *256*, 111–119; b) P. Z. Zhao, T. Tsuchida, *Mater. Sci. Eng. A* **2009**, *499*, 78–82.
- [19] L. Hoffart, U. Heider, L. Jorissen, R. A. Huggins, W. Witschel, *Solid State Ionics* **1994**, *72*, 195–198.
- [20] K. Jun, Y. S. Lee, T. Buonassisi, J. M. Jacobson, *Angew. Chem. Int. Ed.* **2012**, *51*, 423–427; *Angew. Chem.* **2012**, *124*, 438–442.
- [21] T. Yamaguchi, *Catal. Today* **1994**, *20*, 199–217.
- [22] T. C. Li, M. S. Góes, F. Fabregat-Santiago, J. Bisquert, P. R. Bueno, C. Prastichai, J. T. Hupp, T. J. Marks, *J. Phys. Chem. C* **2009**, *113*, 18385–18390.
- [23] H. Dotan, K. Sivula, M. Graetzel, A. Rothschild, S. C. Warren, *Energy Environ. Sci.* **2011**, *4*, 958–964.
- [24] G. Carraro, C. Maccato, A. Gasparotto, K. Kaunisto, C. Sada, D. Barreca, *Plasma Processes Polym.* **2016**, *13*, 191–200.

Received: July 6, 2016

Revised: July 23, 2016

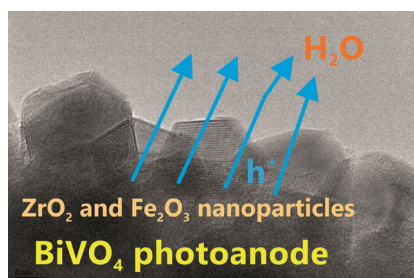
Published online on ■■■■■ 0000

COMMUNICATIONS

M. N. Shaddad, M. A. Ghanem,
A. M. Al-Mayouf, S. Gimenez, J. Bisquert,*
I. Herraiz-Cardona*

■■ - ■■

 Cooperative Catalytic Effect of ZrO_2 and $\alpha\text{-Fe}_2\text{O}_3$ Nanoparticles on BiVO_4 Photoanodes for Enhanced Photoelectrochemical Water Splitting



All the nano things: A combination of ZrO_2 and $\alpha\text{-Fe}_2\text{O}_3$ nanoparticles deposited on the surface of a BiVO_4 film forms a catalytic layer that dramatically enhances the properties of the photoanode for water splitting driven by visible sunlight. A fully reproducible and facile electrolytic synthesis deposition method, which allows remarkably increased performance, indicates attractive implications for technological deployment.